DESY 97-179 ISSN 0418-9833

Low Q^2 Jet Production at HERA and Virtual Photon Structure

H1 Collaboration

Abstract

The transition between photoproduction and deep-inelastic scattering is investigated in jet production at the HERA ep collider, using data collected by the H1 experiment. Measurements of the differential inclusive jet cross-sections $\mathrm{d}\sigma_{ep}/\mathrm{d}E_t^*$ and $\mathrm{d}\sigma_{ep}/\mathrm{d}\eta^*$, where E_t^* and η^* are the transverse energy and the pseudorapidity of the jets in the virtual photon-proton centre of mass frame, are presented for $0 < Q^2 < 49\,\mathrm{GeV}^2$ and $0.3 < y < 0.6$. The interpretation of the results in terms of the structure of the virtual photon is discussed. The data are best described by QCD calculations which include a partonic structure of the virtual photon that evolves with Q^2.

To be submitted to Physics Letters ***B***

C. Adloff[35], S. Aid[13], M. Anderson[23], V. Andreev[26], B. Andrieu[29], V. Arkadov[36], C. Arndt[11], I. Ayyaz[30], A. Babaev[25], J. Bähr[36], J. Bán[18], P. Baranov[26], E. Barrelet[30], R. Barschke[11], W. Bartel[11], U. Bassler[30], M. Beck[14], H.-J. Behrend[11], C. Beier[16], A. Belousov[26], Ch. Berger[1], G. Bernardi[30], G. Bertrand-Coremans[4], R. Beyer[11], P. Biddulph[23], J.C. Bizot[28], K. Borras[8], F. Botterweck[27], V. Boudry[29], S. Bourov[25], A. Braemer[15], W. Braunschweig[1], V. Brisson[28], D.P. Brown[23], W. Brückner[14], P. Bruel[29], D. Bruncko[18], C. Brune[16], J. Bürger[11], F.W. Büsser[13], A. Buniatian[4], S. Burke[19], G. Buschhorn[27], D. Calvet[24], A.J. Campbell[11], T. Carli[27], M. Charlet[11], D. Clarke[5], B. Clerbaux[4], S. Cocks[20], J.G. Contreras[8], C. Cormack[20], J.A. Coughlan[5], M.-C. Cousinou[24], B.E. Cox[23], G. Cozzika[9], D.G. Cussans[5], J. Cvach[31], S. Dagoret[30], J.B. Dainton[20], W.D. Dau[17], K. Daum[40], M. David[9], A. De Roeck[11], E.A. De Wolf[4], B. Delcourt[28], M. Dirkmann[8], P. Dixon[19], W. Dlugosz[7], K.T. Donovan[21], J.D. Dowell[3], A. Droutskoi[25], J. Ebert[35], T.R. Ebert[20], G. Eckerlin[11], V. Efremenko[25], S. Egli[38], R. Eichler[37], F. Eisele[15], E. Eisenhandler[21], E. Elsen[11], M. Erdmann[15], A.B. Fahr[13], L. Favart[28], A. Fedotov[25], R. Felst[11], J. Feltesse[9], J. Ferencei[18], F. Ferrarotto[33], K. Flamm[11], M. Fleischer[8], M. Flieser[27], G. Flügge[2], A. Fomenko[26], J. Formánek[32], J.M. Foster[23], G. Franke[11], E. Gabathuler[20], K. Gabathuler[34], F. Gaede[27], J. Garvey[3], J. Gayler[11], M. Gebauer[36], R. Gerhards[11], A. Glazov[36], L. Goerlich[6], N. Gogitidze[26], M. Goldberg[30], B. Gonzalez-Pineiro[30], I. Gorelov[25], C. Grab[37], H. Grässler[2], T. Greenshaw[20], R.K. Griffiths[21], G. Grindhammer[27], A. Gruber[27], C. Gruber[17], T. Hadig[1], D. Haidt[11], L. Hajduk[6], T. Haller[14], M. Hampel[1], W.J. Haynes[5], B. Heinemann[11], G. Heinzelmann[13], R.C.W. Henderson[19], S. Hengstmann[38], H. Henschel[36], I. Herynek[31], M.F. Hess[27], K. Hewitt[3], K.H. Hiller[36], C.D. Hilton[23], J. Hladký[31], M. Höppner[8], D. Hoffmann[11], T. Holtom[20], R. Horisberger[34], V.L. Hudgson[3], M. Hütte[8], M. Ibbotson[23], Ç. İşsever[8], H. Itterbeck[1], M. Jacquet[28], M. Jaffre[28], J. Janoth[16], D.M. Jansen[14], L. Jönsson[22], D.P. Johnson[4], H. Jung[22], P.I.P. Kalmus[21], M. Kander[11], D. Kant[21], U. Kathage[17], J. Katzy[15], H.H. Kaufmann[36], O. Kaufmann[15], M. Kausch[11], S. Kazarian[11], I.R. Kenyon[3], S. Kermiche[24], C. Keuker[1], C. Kiesling[27], M. Klein[36], C. Kleinwort[11], G. Knies[11], J.H. Köhne[27], H. Kolanoski[39], S.D. Kolya[23], V. Korbel[11], P. Kostka[36], S.K. Kotelnikov[26], T. Krämerkämper[8], M.W. Krasny[6,30], H. Krehbiel[11], D. Krücker[27], A. Küpper[35], H. Küster[22], M. Kuhlen[27], T. Kurča[36], B. Laforge[9], R. Lahmann[11], M.P.J. Landon[21], W. Lange[36], U. Langenegger[37], A. Lebedev[26], F. Lehner[11], V. Lemaitre[11], S. Levonian[29], M. Lindstroem[22], J. Lipinski[11], B. List[11], G. Lobo[28], G.C. Lopez[12], V. Lubimov[25], D. Lüke[8,11], L. Lytkin[14], N. Magnussen[35], H. Mahlke-Krüger[11], E. Malinovski[26], R. Maraček[18], P. Marage[4], J. Marks[15], R. Marshall[23], J. Martens[35], G. Martin[13], R. Martin[20], H.-U. Martyn[1], J. Martyniak[6], T. Mavroidis[21], S.J. Maxfield[20], S.J. McMahon[20], A. Mehta[5], K. Meier[16], P. Merkel[11], F. Metlica[14], A. Meyer[11], A. Meyer[13], H. Meyer[35], J. Meyer[11], P.-O. Meyer[2], A. Migliori[29], S. Mikocki[6], D. Milstead[20], J. Moeck[27], F. Moreau[29], J.V. Morris[5], E. Mroczko[6], D. Müller[38], K. Müller[11], P. Murín[18], V. Nagovizin[25], R. Nahnhauer[36], B. Naroska[13], Th. Naumann[36], I. Négri[24], P.R. Newman[3], D. Newton[19], H.K. Nguyen[30], T.C. Nicholls[3], F. Niebergall[13], C. Niebuhr[11], Ch. Niedzballa[1], H. Niggli[37], G. Nowak[6], T. Nunnemann[14], H. Oberlack[27], J.E. Olsson[11], D. Ozerov[25], P. Palmen[2], E. Panaro[11], A. Panitch[4], C. Pascaud[28], S. Passaggio[37], G.D. Patel[20], H. Pawletta[2], E. Peppel[36], E. Perez[9], J.P. Phillips[20], A. Pieuchot[24], D. Pitzl[37], R. Pöschl[8], G. Pope[7], B. Povh[14], K. Rabbertz[1], P. Reimer[31], H. Rick[8], S. Riess[13], E. Rizvi[11], P. Robmann[38], R. Roosen[4], K. Rosenbauer[1], A. Rostovtsev[30], F. Rouse[7], C. Royon[9], K. Rüter[27], S. Rusakov[26], K. Rybicki[6], D.P.C. Sankey[5], P. Schacht[27], J. Scheins[1], S. Schiek[11], S. Schleif[16], P. Schleper[15], W. von Schlippe[21], D. Schmidt[35], G. Schmidt[11], L. Schoeffel[9], A. Schöning[11], V. Schröder[11], E. Schuhmann[27], H.-C. Schultz-Coulon[11], B. Schwab[15], F. Sefkow[38], A. Semenov[25], V. Shekelyan[11], I. Sheviakov[26], L.N. Shtarkov[26], G. Siegmon[17], U. Siewert[17], Y. Sirois[29], I.O. Skillicorn[10], T. Sloan[19], P. Smirnov[26], M. Smith[20], V. Solochenko[25], Y. Soloviev[26], A. Specka[29], J. Spiekermann[8], S. Spielman[29], H. Spitzer[13], F. Squinabol[28], P. Steffen[11], R. Steinberg[2], J. Steinhart[13], B. Stella[33], A. Stellberger[16], J. Stiewe[16], K. Stolze[36], U. Straumann[15], W. Struczinski[2], J.P. Sutton[3], M. Swart[16],

S. Tapprogge[16], M. Taševský[32], V. Tchernyshov[25], S. Tchetchelnitski[25], J. Theissen[2], G. Thompson[21], P.D. Thompson[3], N. Tobien[11], R. Todenhagen[14], P. Truöl[38], J. Zálešák[32], G. Tsipolitis[37], J. Turnau[6], E. Tzamariudaki[11], P. Uelkes[2], A. Usik[26], S. Valkár[32], A. Valkárová[32], C. Vallée[24], P. Van Esch[4], P. Van Mechelen[4], D. Vandenplas[29], Y. Vazdik[26], P. Verrecchia[9], G. Villet[9], K. Wacker[8], A. Wagener[2], M. Wagener[34], R. Wallny[15], T. Walter[38], B. Waugh[23], G. Weber[13], M. Weber[16], D. Wegener[8], A. Wegner[27], T. Wengler[15], M. Werner[15], L.R. West[3], S. Wiesand[35], T. Wilksen[11], S. Willard[7], M. Winde[36], G.-G. Winter[11], C. Wittek[13], M. Wobisch[2], H. Wollatz[11], E. Wünsch[11], J. Žáček[32], D. Zarbock[12], Z. Zhang[28], A. Zhokin[25], P. Zini[30], F. Zomer[28], J. Zsembery[9], and M. zurNedden[38],

[1] I. Physikalisches Institut der RWTH, Aachen, Germany[a]
[2] III. Physikalisches Institut der RWTH, Aachen, Germany[a]
[3] School of Physics and Space Research, University of Birmingham, Birmingham, UK[b]
[4] Inter-University Institute for High Energies ULB-VUB, Brussels; Universitaire Instelling Antwerpen, Wilrijk; Belgium[c]
[5] Rutherford Appleton Laboratory, Chilton, Didcot, UK[b]
[6] Institute for Nuclear Physics, Cracow, Poland[d]
[7] Physics Department and IIRPA, University of California, Davis, California, USA[e]
[8] Institut für Physik, Universität Dortmund, Dortmund, Germany[a]
[9] DSM/DAPNIA, CEA/Saclay, Gif-sur-Yvette, France
[10] Department of Physics and Astronomy, University of Glasgow, Glasgow, UK[b]
[11] DESY, Hamburg, Germany[a]
[12] I. Institut für Experimentalphysik, Universität Hamburg, Hamburg, Germany[a]
[13] II. Institut für Experimentalphysik, Universität Hamburg, Hamburg, Germany[a]
[14] Max-Planck-Institut für Kernphysik, Heidelberg, Germany[a]
[15] Physikalisches Institut, Universität Heidelberg, Heidelberg, Germany[a]
[16] Institut für Hochenergiephysik, Universität Heidelberg, Heidelberg, Germany[a]
[17] Institut für Reine und Angewandte Kernphysik, Universität Kiel, Kiel, Germany[a]
[18] Institute of Experimental Physics, Slovak Academy of Sciences, Košice, Slovak Republic[f,j]
[19] School of Physics and Chemistry, University of Lancaster, Lancaster, UK[b]
[20] Department of Physics, University of Liverpool, Liverpool, UK[b]
[21] Queen Mary and Westfield College, London, UK[b]
[22] Physics Department, University of Lund, Lund, Sweden[g]
[23] Physics Department, University of Manchester, Manchester, UK[b]
[24] CPPM, Université d'Aix-Marseille II, IN2P3-CNRS, Marseille, France
[25] Institute for Theoretical and Experimental Physics, Moscow, Russia
[26] Lebedev Physical Institute, Moscow, Russia[f]
[27] Max-Planck-Institut für Physik, München, Germany[a]
[28] LAL, Université de Paris-Sud, IN2P3-CNRS, Orsay, France
[29] LPNHE, Ecole Polytechnique, IN2P3-CNRS, Palaiseau, France
[30] LPNHE, Universités Paris VI and VII, IN2P3-CNRS, Paris, France
[31] Institute of Physics, Czech Academy of Sciences of the Czech Republic, Praha, Czech Republic[f,h]
[32] Nuclear Center, Charles University, Praha, Czech Republic[f,h]
[33] INFN Roma 1 and Dipartimento di Fisica, Università Roma 3, Roma, Italy
[34] Paul Scherrer Institut, Villigen, Switzerland
[35] Fachbereich Physik, Bergische Universität Gesamthochschule Wuppertal, Wuppertal, Germany[a]
[36] DESY, Institut für Hochenergiephysik, Zeuthen, Germany[a]
[37] Institut für Teilchenphysik, ETH, Zürich, Switzerland[i]
[38] Physik-Institut der Universität Zürich, Zürich, Switzerland[i]
[39] Institut für Physik, Humboldt-Universität, Berlin, Germany[a]

[40] Rechenzentrum, Bergische Universität Gesamthochschule Wuppertal, Wuppertal, Germany[a]

[a] Supported by the Bundesministerium für Bildung, Wissenschaft, Forschung und Technologie, FRG, under contract numbers 7AC17P, 7AC47P, 7DO55P, 7HH17I, 7HH27P, 7HD17P, 7HD27P, 7KI17I, 6MP17I and 7WT87P
[b] Supported by the UK Particle Physics and Astronomy Research Council, and formerly by the UK Science and Engineering Research Council
[c] Supported by FNRS-NFWO, IISN-IIKW
[d] Partially supported by the Polish State Committee for Scientific Research, grant no. 2P03B 055 13
[e] Supported in part by USDOE grant DE F603 91ER40674
[f] Supported by the Deutsche Forschungsgemeinschaft
[g] Supported by the Swedish Natural Science Research Council
[h] Supported by GA ČR grant no. 202/96/0214, GA AV ČR grant no. A1010619 and GA UK grant no. 177
[i] Supported by the Swiss National Science Foundation
[j] Supported by VEGA SR grant no. 2/1325/96

1 Introduction and Motivation

In this paper jet production in electron-proton scattering in the transition region between photoproduction and deep inelastic scattering (DIS) is investigated. The results are interpreted in terms of parton densities of the virtual photon which are probed at a scale determined by the transverse momentum (p_t) of the jets and which evolve with the virtuality of the photon (Q^2).

In the photoproduction of jets [1], the photon can couple directly to a parton from the proton ("direct" interactions). However, the cross-section is dominated by interactions, so-called "resolved" processes, in which the photon fluctuates into a system of partons and one of these interacts with a parton out of the proton to produce the jets. This separation into direct and resolved processes can only be made unambiguously in leading order [2]. At its simplest, the hadronic fluctuation of the photon may take the form of a quark–antiquark ($q\bar{q}$) pair. More complicated structure is built up through QCD interactions. In addition to this point-like "anomalous" component [3], the photon can also acquire a more conventional hadronic structure, often modelled as a fluctuation into a vector meson (vector dominance model, VDM). The cross-section for jet production can be expressed as a convolution of universal parton densities of the proton and the photon together with hard parton-parton scattering cross-sections. The evolution of the photon parton densities with the scale at which they are probed can be calculated in perturbative QCD and has been extensively measured in two-photon interactions [4] and recently at HERA [5].

In contrast, it is usual to consider that the only contribution to jet production in DIS is from direct interactions with the partons in the proton probed by a structureless photon at the scale Q^2. However, in the small region of phase space where high p_t jets are produced with p_t^2 much larger than Q^2, it is possible that the jet production may be most easily understood in terms of the partonic structure of the virtual photon together with that of the proton [6, 7, 8, 9]. Parton densities within the virtual photon are expected to be suppressed [7, 10, 11, 12, 13] with increasing Q^2 until direct processes dominate at $Q^2 \sim p_t^2$. Measurements of the virtual photon structure in two-photon interactions require detection of both scattered leptons at non-zero scattering angles. Only one such measurement has previously been made [14]. The extensive Q^2 range together with the large centre-of-mass energy available at HERA enables a detailed study of the Q^2 evolution of photon structure.

After a description of the data used in this analysis, different models are introduced which are intended to describe the photoproduction and deep inelastic scattering regimes. The inclusive differential jet cross-sections are then presented as a function of jet transverse energy and rapidity for photon virtualities in the range $0 < Q^2 < 49\,\mathrm{GeV}^2$. Finally, a measurement of the energy flow in the direction of the photon is shown as a function of Q^2 to verify the existence of a photon remnant.

2 The H1 Detector

A full description of the H1 detector can be found elsewhere [15] and only those components relevant for this analysis are described here.

The coordinate system used has the nominal interaction point as the origin and the incident proton beam defining the $+z$ direction. The polar angle θ is defined with respect to the proton direction, and the pseudorapidity is given by $\eta = -\ln\tan(\theta/2)$.

A finely grained Liquid Argon calorimeter [16] covers the range in polar angle $4^\circ < \theta < 154^\circ$, with full azimuthal acceptance. It consists of an electromagnetic section with lead absorbers,

20–30 radiation lengths in depth, and a hadronic section with steel absorbers. The total depth of the calorimeter ranges from 4.5 to 8 hadronic interaction lengths. The energy resolution is $\sigma(E)/E \approx 0.11/\sqrt{E}$ for electrons and $\sigma(E)/E \approx 0.5/\sqrt{E}$ for pions (E in GeV), as measured in test beams [17]. The absolute energy scale is known to a precision of 3% for electrons and 4% for hadrons.

A series of interleaved drift and multiwire proportional chambers surround the interaction point, enabling the reconstruction of charged particles in the range $7° < \theta < 165°$, and the determination of the event vertex. A uniform axial magnetic field of 1.15 T is provided by a superconducting coil which surrounds the calorimeter.

For 1994 data taking, the polar region $151° < \theta < 176°$ was covered by the BEMC [18], a lead/scintillator electromagnetic calorimeter with a depth of 21.7 radiation lengths. The resolution was given by $0.10/\sqrt{E}$ (E in GeV) and the absolute electromagnetic energy scale was known to a precision of about 1%. In 1995, the BEMC was replaced by the SPACAL [19], a lead/scintillating fiber calorimeter with both an electromagnetic and hadronic section covering the range $153° < \theta < 177.8°$. The energy resolution for the electromagnetic section has been determined as $7.5\%/\sqrt{E}(\mathrm{GeV}) \oplus 2.5\%$ and the absolute energy scale uncertainty is 1% at 27.5 GeV and 3% at 7 GeV [20]. The hadronic energy scale uncertainty of the measurement in the SPACAL is presently about 10%. Both calorimeter sections have a time resolution better than 1 ns, enabling the reduction of proton beam induced background events. The BEMC and the SPACAL were used both to trigger on and to measure the scattered lepton in DIS processes for $0.65 < Q^2 < 49\,\mathrm{GeV}^2$.

In 1994, the backward proportional chamber (BPC) was located in front of the BEMC. In 1995, this was replaced by a four module drift chamber, the BDC [21], in front of the SPACAL. The polar angle of the scattered lepton was determined using the event vertex and information from these backward tracking chambers.

The luminosity system consists of two crystal calorimeters with resolution $\sigma(E)/E = 0.1/\sqrt{E}$ (E in GeV). The electron tagger is located at $z = -33$ m and the photon detector at $z = -103$ m. The electron tagger accepts electrons with an energy of between 0.2 and 0.8 of the incident beam energy, and with scattering angles $\theta' < 5$ mrad ($\theta' = \pi - \theta$).

3 Data Samples and Event Selection

The analysis is based on data taken by the H1 experiment in 1994 and 1995. Three data samples were used, each restricted to a region of Q^2 with good acceptance:

- $Q^2 < 10^{-2}\,\mathrm{GeV}^2$: The photoproduction sample in which the scattered electron is detected in the electron tagger of the luminosity system. The events were triggered by demanding an energy deposit in the electron tagger with $E > 4$ GeV in coincidence with at least one track pointing to the vertex region ($p_t \gtrsim 500$ MeV). More details of the trigger conditions can be found in [22]. The data sample used was a sub-sample of that collected in 1994 and corresponds to an integrated luminosity of 210 nb^{-1}.

- $0.65 < Q^2 < 20\,\mathrm{GeV}^2$: The 1995 shifted vertex data sample, corresponding to 120 nb^{-1} collected in a special run in which the mean position of the interaction point was shifted by 70 cm in the $+z$ direction, enabling positron detection in the SPACAL down to angles of 178.5°. The events were triggered by requiring a cluster of more than 5 GeV in the SPACAL and timing consistent with an ep bunch crossing. The most energetic cluster in the electromagnetic section of the SPACAL was taken as the electron candidate [20].

- $9 < Q^2 < 49\,\mathrm{GeV}^2$: The standard 1994 data sample, corresponding to an integrated luminosity of 2 pb^{-1}. The events were triggered by requiring a cluster of more than 4 GeV in the BEMC, and the scattered positron was taken as the most energetic BEMC cluster [23].

The error on the luminosity determination was 1.5(3)% for data taken in 1994(1995). For all three samples, the z position of the interaction vertex was required to be within 30 cm of the nominal position. In addition, to enable comparisons between the DIS and photoproduction data, for all data samples the inelasticity variable y was restricted to $0.3 < y < 0.6$, the range where the acceptance of the electron tagger is well-understood.

For events with $0.65 < Q^2 < 49\,\mathrm{GeV}^2$ it was also required that the $\sum_i (E_i - P_{zi})$ of all the reconstructed calorimeter clusters, which should be equal to twice the electron beam energy for a DIS event, was greater than 45 GeV. Monte Carlo studies showed that the background from real photoproduction events where hadronic activity in the backward region fakes a scattered lepton was reduced to less than 3% in the selected kinematic region.

The event kinematics were reconstructed from the scattered electron 4–vector. Jets were reconstructed in the $\gamma^* p$ centre of mass frame using a k_T clustering algorithm [24]. The merging procedure is based on the quantity y_{ki} which is evaluated for each pair of clusters:

$$y_{ki} = \frac{2(1-\cos\theta_{ki})}{E_{cut}^2} \min(E_k^2, E_i^2) \qquad (1)$$

where E_k and E_i are the energies of the clusters and θ_{ki} is the angle between them. In addition, to enable the association of particles to either a photon or proton remnant, two infinite momentum pseudo–particles along $\pm z$ are included in the clustering procedure, but excluded from the final jets. Particles are combined by the addition of their 4–vectors when $y_{ki} < 1$. Thus E_{cut} sets the scale for the jet resolution and separates the hard jets from the beam remnants. In this analysis, E_{cut} was chosen to be 3 GeV.

Jets were accepted with a transverse energy $E_t^* > 4\,\mathrm{GeV}$ and a pseudorapidity in the range $-2.5 < \eta^* < -0.5$, where E_t^* and η^* are calculated in the $\gamma^* p$ frame with positive η^* corresponding to the incident proton direction. For the photoproduction sample, the E_t^* threshold was raised to 5 GeV to reduce the influence of multiple parton interactions. This selection ensures that the energy flow around the jet axis is well described by the Monte Carlo models used for the acceptance corrections.

4 QCD Motivated Calculations

For acceptance corrections and comparisons with the measured jet cross-sections, several event generators were used.

The PHOJET 1.03 [25] generator simulates all relevant components of the total photoproduction cross-section. It is based on the two-component Dual Parton Model [26] and incorporates both hard and multiple soft interactions. The photon flux is calculated using the Weizsäcker–Williams approximation [27, 28] and the hard processes are calculated using leading order QCD matrix elements. Final state QCD radiation and fragmentation effects are implemented using the string fragmentation model JETSET 7.4 [29]. In this analysis, PHOJET was used to simulate quasi-real photon-proton interactions.

DIS events were modelled using the LEPTO 6.5 [30] and ARIADNE 4.08 [31] programs. LEPTO includes the first order QCD matrix elements and uses leading-log parton showers to

model higher order radiation. The ARIADNE generator uses the Colour Dipole model [32] to simulate QCD radiation to all orders. A feature of this model is that the hard subprocess need not be generated at the photon vertex, and this can be regarded as generating "resolved-like" events. For both models, hadronisation is performed using JETSET.

HERWIG 5.9 [33] was used to model direct and resolved photon processes. The emission of the photon from the incident electron is generated according to the equivalent photon approximation [28]. The parton-parton interactions are simulated according to leading order QCD calculations, and a parton shower model which effectively includes interference effects between the initial and final state showers (colour coherence) is implemented [34]. The factorisation scales were set according to the transverse momentum of the scattered partons, with a cut-off at $p_t^{min} = 1.5\,\mathrm{GeV}$. A cluster model is used for hadronisation.

HERWIG includes the option of additional interactions of the beam remnant in the phenomenological soft underlying event model. A reasonable description of the jet profiles and the jet rates observed in the data was obtained with no soft underlying event for $Q^2 > 0.65\,\mathrm{GeV}^2$ and with a soft underlying event in 15% of the resolved interactions at $Q^2 = 0\,\mathrm{GeV}^2$. These values were used throughout the subsequent analysis.

The RAPGAP Monte Carlo [35] originally developed to simulate diffractive processes, also includes modeling of deep-inelastic and all relevant resolved photon processes. DIS processes are simulated using leading order QCD matrix elements with a p_t^2 cut-off scheme for the light quarks and the full matrix element for heavy quarks. For resolved photon processes, the equivalent photon approximation is used to model the flux of virtual photons. Parton-parton interactions are calculated from on-shell matrix elements supplemented by initial and final state parton showers.

Both HERWIG and RAPGAP include models for the evolution of the photon parton densities with Q^2. Three approaches are considered. The first assumes no Q^2 dependence of the parton densities. The second uses the Drees-Godbole parameterization [12] of virtual photon structure, following an analysis of Borzumati and Schuler [13], in which the quark densities $f_{q|\gamma^*}$ in a photon of virtuality Q^2 probed at a scale p_t^2 are related to those of a real photon $f_{q|\gamma}$ by:

$$f_{q|\gamma^*}(x, p_t^2, Q^2) = f_{q|\gamma}(x, p_t^2)\; L(p_t^2, Q^2, \omega) \tag{2}$$

$$= f_{q|\gamma}(x, p_t^2) \frac{\ln\left\{(p_t^2+\omega^2)/(Q^2+\omega^2)\right\}}{\ln\left\{(p_t^2+\omega^2)/\omega^2\right\}} \tag{3}$$

An analogous relation exists for the gluon density, with L replaced by L^2. The parameter ω is the value of Q^2 above which the suppression becomes significant. We use a value of $\omega^2 = 1\,\mathrm{GeV}^2$ and the GRV-G HO (DIS) [36] parameterizations for the unsuppressed photon parton densities. Throughout this paper we refer to this as the DG model. The third approach is to use the photon parton densities from Schuler and Sjöstrand [37] (SaS) which are valid for $Q^2 \geq 0\,\mathrm{GeV}^2$. In this scheme, the photon parton densities are decomposed into a direct, a VDM and a perturbative anomalous component. We will show comparisons with the SaS-2D parameterisation in the DIS scheme using the form for the Q^2 suppression recommended by the authors.

All models were used with the GRV94 HO (DIS) [38] parton densities for the proton, which give a good description of the measured F_2 for $Q^2 > 1\,\mathrm{GeV}^2$ [20].

5 Inclusive Jet Cross-Section

5.1 Determination

The distributions of the jet transverse energy (E_t^*) and pseudorapidity (η^*) in the $\gamma^* p$ centre of mass frame were corrected bin-by-bin for detector effects using generated events passed through

a simulation of the H1 detector based on the GEANT program [39]. The bin sizes were chosen to keep the effects of finite resolution and bin-to-bin migration small. For the photoproduction data, correction factors were determined from the HERWIG DG model, which gives a good description of the data. The model dependence was estimated by comparison with the values obtained from PHOJET, which also gives a good description of the jets observed in the data. This model dependence is one of the largest contributions to the systematic error. For the DIS data, correction factors in the range $0.65 < Q^2 < 20\,\mathrm{GeV}^2$ were determined from the HERWIG DG model, and for $Q^2 > 20\,\mathrm{GeV}^2$ from the HERWIG direct model, both of which give a satisfactory description of the observed jets in these kinematic regimes. LEPTO was used to estimate the model dependence of the correction factors, which is again one of the dominant sources of systematic error.

The other large source of systematic error arises from the uncertainty in the knowledge of the hadronic energy scale of the Liquid Argon calorimeter. This has two contributions; a possible 3% variation in the energy scale between different calorimeter modules, which is included in the point–to–point error, and a 4% uncertainty in the overall energy scale, which affects the normalisation of the jet cross-sections.

Further sources of systematic error include a 1(2)% uncertainty in the electromagnetic energy scale of the BEMC(SPACAL) and a 1 mrad uncertainty in the polar angle of the scattered electron. For the photoproduction data, the uncertainty in the acceptance and energy calibration of the electron tagger was included. A 20(10)% uncertainty in the knowledge of the hadronic energy scale of the BEMC(SPACAL) is also considered. The 1.5(3)% uncertainty in the luminosity determination in 1994(1995) affects the overall normalisation of the jet cross-sections.

The effect of radiative corrections in DIS events has been studied using the HERACLES program [40] which includes complete first order radiative corrections and the emission of real bremsstrahlung photons for the electroweak interaction. The effect is 20–30% for jets with E_t^* of 4 GeV, decreases with increasing E_t^* and is negligible for $E_t^* > 7\,\mathrm{GeV}$. It does not significantly influence the conclusions and the data are not corrected for this effect.

The corrected cross-sections obtained from the 1995 shifted vertex data and from the 1994 data are in good agreement in the region $9 < Q^2 < 20\,\mathrm{GeV}^2$ where the data samples overlap.

5.2 Results

Figure 1 shows the inclusive ep jet cross–section $\mathrm{d}\sigma_{ep}/\mathrm{d}E_t^*$ for $0.3 < y < 0.6$ and jets with $-2.5 < \eta^* < -0.5$, and the values are listed in table 2. The data are compared with the prediction from the HERWIG DG model, which includes a resolved component of the virtual photon. This is able to give a good description of the data except for jets in the lowest E_t^* range when $9 < Q^2 < 49\,\mathrm{GeV}^2$. Also shown is the direct contribution to this model which accounts for an increasing fraction of the total prediction as Q^2 increases, but which alone cannot describe the measured jet cross-sections.

The jet cross-section $\mathrm{d}\sigma_{ep}/\mathrm{d}\eta^*$ for jets with $E_t^* > 5\,\mathrm{GeV}$ is shown in figure 2 and the values are listed in table 3. The data are compared to the HERWIG DG model and the direct photon contribution to this model. The direct photon processes alone significantly underestimate the jet cross-section at low Q^2, but the data are described by HERWIG if the resolved photon component is included and suppressed with increasing Q^2 according to the DG model. The relative contribution to the jet cross-section from resolved photon processes increases towards the proton ($+\eta^*$) direction.

Q^2 (GeV^2)	Flux factor
$< 10^{-2}$	1.16×10^{-2}
$0.65 < Q^2 < 1.2$	6.56×10^{-4}
$1.2 < Q^2 < 2.6$	8.27×10^{-4}
$2.6 < Q^2 < 4$	4.61×10^{-4}
$4 < Q^2 < 9$	8.68×10^{-4}
$9 < Q^2 < 20$	8.54×10^{-4}
$20 < Q^2 < 25$	2.39×10^{-4}
$25 < Q^2 < 36$	3.90×10^{-4}
$36 < Q^2 < 49$	3.30×10^{-4}

Table 1: The flux factors used for the calculation of the $\gamma^* p$ jet cross-sections (see equation 5).

In order to study in more detail the Q^2 evolution of the photon parton densities, we factor out the Q^2 dependence contained in the flux of photons and calculate a $\gamma^* p$ jet cross-section in each Q^2 range using:

$$\sigma_{\gamma^* p \to jet+X} = \frac{\sigma_{ep \to e+jet+X}}{F_{\gamma|e}} \tag{4}$$

We use the Weizsäcker–Williams approximation [27, 28] to calculate the flux of photons, $F_{\gamma|e}$:

$$F_{\gamma|e} = \int_{y_{min}}^{y_{max}} \mathrm{d}y \int_{Q^2_{min}}^{Q^2_{max}} \mathrm{d}Q^2 f_{\gamma|e}(y, Q^2) \tag{5}$$

with

$$f_{\gamma|e}(y, Q^2) = \frac{\alpha}{2\pi Q^2} \left\{ \frac{1 + (1-y)^2}{y} - \frac{2(1-y)}{y} \frac{Q^2_{min}}{Q^2} \right\} \tag{6}$$

The flux is integrated over $0.3 < y < 0.6$ and Q^2_{max} and Q^2_{min} are the upper and lower edges of the Q^2 range. For photoproduction:

$$Q^2_{min} = \frac{m_e^2 y^2}{1-y} \tag{7}$$

where m_e is the electron mass.

This factorisation of the cross-section remains a reasonable approximation for high p_t jet production if $p_t^2 \gg Q^2$ [7], a condition which is satisfied by the majority of our data[1]. The numerical values of the flux factors used in each Q^2 range are listed in table 1.

The Q^2 dependence of the inclusive $\gamma^* p$ jet cross-section at fixed jet E_t^* is shown in figure 3. For $E_t^* < 10\,\mathrm{GeV}$ there is a significant decrease of the jet cross-section with increasing Q^2. Also shown for comparison are the predictions from LEPTO and ARIADNE. We expect such DIS models to be valid when $Q^2 \gtrsim E_t^{*2}$, where the photon cannot be resolved. This region corresponds to the 2–3 highest Q^2 ranges in figures 3a and 3b. It can be seen that both models give an adequate description of the data in these ranges. However, neither model can describe the data when $Q^2 < E_t^{*2}$ and the virtual photon can be resolved. Also the predictions of these models differ significantly in this region. Although ARIADNE predicts a jet cross-section which decreases with increasing Q^2 in a similar manner to the data and is able to describe the data for $Q^2 \gtrsim 4\,\mathrm{GeV}^2$, it is unable to describe the data at all E_t^* and all Q^2. The prediction from

[1] We continue to use (4) as a formal definition of the $\gamma^* p$ cross-section for all p_t^2 and Q^2.

ARIADNE is sensitive to the parameters which limit the phase space for QCD radiation[2] and therefore to the fraction of "resolved-like" events produced by the model, but we found no choice of these parameters which enabled the model to describe the data.

The same data compared to a series of models which include a partonic structure for the virtual photon, as implemented in the HERWIG and RAPGAP generators, are shown in figure 4. In each case, the sum of the direct and resolved contributions is shown. The dot–dashed curve shows the prediction from HERWIG assuming the GRV-G HO structure function for the photon with no Q^2 suppression. The resulting $\gamma^* p$ jet cross-section is almost independent of Q^2, in contrast to the data which show, except for the highest E_t^* jets, a significant decrease of the jet cross-section with Q^2. The jet cross-section predicted by this model at $Q^2 = 0\,\mathrm{GeV}^2$ is slightly larger than that predicted for $Q^2 > 0\,\mathrm{GeV}^2$ because a soft underlying event is included at $Q^2 = 0\,\mathrm{GeV}^2$. Also shown are the predictions from HERWIG and from RAPGAP using the DG model for the virtual photon structure. The models are in good agreement with each other, and describe the data well except for jets with $4 < E_t^* < 5\,\mathrm{GeV}$ when $9 < Q^2 < 49\,\mathrm{GeV}^2$, where they underestimate the measured cross-section. We note that in the DG model the photon parton density functions all vanish for $Q^2 > p_t^2$, which is approximately the case in this region. The data are best described by the RAPGAP model using the SaS-2D parameterization of the virtual photon. In contrast to the DG model, the photon parton densities do not vanish when $Q^2 > p_t^2$ in this parameterization.

The inclusive jet cross-section can therefore be understood if a partonic structure is ascribed to the virtual photon. Moreover, the observed Q^2 evolution of the jet cross-sections can be explained by the suppression of the parton densities with increasing photon virtuality as predicted by QCD inspired models. For $Q^2 \gtrsim p_t^2$, the photon is effectively structureless.

6 Photon Remnant

The jet algorithm used in this analysis assigns particles to a photon remnant. The fraction of the incident photon's energy which is reconstructed in the photon remnant jet is given by:

$$f = \frac{\sum_i E_i^*}{E_e^* - E_e'^*}$$

where E_i^* is the energy of a particle assigned to the photon remnant and E_e^* and $E_e'*$ are the energies of the incident and scattered electron respectively in the $\gamma^* p$ frame.

Figure 5 shows the uncorrected distribution of f in the data, as a function of Q^2, for events with at least one jet with $E_t^* > 5\,\mathrm{GeV}$ and $-2.5 < \eta^* < -0.5$. At $Q^2 = 0\,\mathrm{GeV}^2$, where resolved photon processes dominate the cross-section, most of the events with jets also contain a photon remnant with a significant fraction of the incident photon's energy. Conversely, at the highest Q^2 values, where the direct processes dominate, f is peaked at zero. Also shown are the predictions from the HERWIG DG model and from LEPTO after detector simulation. It can be seen that the distribution of f from LEPTO is peaked at zero for all Q^2, as expected for a model which includes only direct processes. At low Q^2, the data agree with the HERWIG DG model, and at high Q^2 they agree with the LEPTO prediction.

The evolution of f with Q^2 is consistent with the picture of a resolved photon contribution which is suppressed with increasing virtuality.

[2]PARA(10) and PARA(15). We use PARA(10)=1.5 and PARA(15)=0.5 by default.

7 Conclusions

The inclusive ep jet cross-sections $\mathrm{d}\sigma_{ep}/\mathrm{d}E_t^*$ and $\mathrm{d}\sigma_{ep}/\mathrm{d}\eta^*$ have been measured in the kinematic range $0.3 < y < 0.6$ and $0 < Q^2 < 49$ GeV^2 .

Models in which the photon only couples directly to the partons of the hard scattering process fail to describe the data in the region $E_t^{*2} \gtrsim Q^2$, where the virtual photon can be resolved. Models which include a resolved component of the photon suppressed with Q^2 are in good agreement with the data. The best description of the data was obtained with a model which includes direct, VDM and perturbative contributions to the virtual photon structure.

It has been established that the energy assigned to the photon remnant in events with high E_t^* jets is on average large at low Q^2 and decreases with increasing Q^2, consistent with the picture of a resolved photon component which is suppressed with its increasing virtuality.

Acknowledgements

We are grateful to the HERA machine group whose outstanding efforts have made and continue to make this experiment possible. We thank the engineers and technicians for their work in constructing and now maintaining the H1 detector, our funding agencies for financial support, the DESY technical staff for continual assistance, and the DESY directorate for the hospitality which they extend to the non-DESY members of the collaboration.

References

[1] ZEUS Collab., M. Derrick et al., Phys. Lett. **B322** (1994) 287.
H1 Collab., T. Ahmed et al., Nucl. Phys. **B445**(1995) 195.
H1 Collab., S. Aid et al., Z. Phys. **C70** (1996) 17.
ZEUS Collab., M. Derrick et al., Phys. Lett. **B384** (1996) 401.
For a recent review see for example:
M. Erdmann, *The Partonic Structure of the Photon*, Springer STMP 138 (1997).

[2] J. Chýla, Phys. Lett. **B320** (1994) 186.

[3] E. Witten, Nucl. Phys. **B120** (1977) 189.

[4] PLUTO Collab., Ch. Berger et al., Phys. Lett. **B142** (1984) 111.
PLUTO Collab., Ch. Berger et al., Nucl. Phys. **B281** (1987) 365.
PLUTO Collab., Ch. Berger et al., Phys. Lett. **107B** (1981) 168.
JADE Collab., W. Bartel et al., Z. Phys. **C24** (1984) 231.
TASSO Collab., M. Althoff et al., Z. Phys. **C24** (1984) 231.
TPC/2γ Collab., H. Aihara et al. Phys. Rev. Lett. **58** (1987) 97.
TPC/2γ Collab., H. Aihara et al. Z. Phys. **C34** (1987) 1.
CELLO Collab., H. J. Berend et al., contributed to the XXVth Int. Conf. on HEP, Singapore 1990, unpublished.
AMY Collab., T. Sasaki et al., Phys. Lett. **B252** (1990) 491.
OPAL Collab., R. Akers et al., Z. Phys. **C61** (1994) 199.
AMY Collab., B. J. Kim et al., Phys. Lett. **B325** (1994) 248.
TOPAZ Collab., H. Hayashii et al., Phys. Lett. **B314** (1993) 149.
ALEPH Collab., D. Buskulic et al., Phys. Lett. **B313** (1993) 509.
DELPHI Collab., P. Abreu et al., Phys. Lett. **B342** (1995) 402.

OPAL Collab., K. Ackerstaff, et al., Z. Phys. **C74** (1997) 33.
For recent reviews, see for example:
A. Vogt, Proc. of the Workshop on Two-Photon Physics at LEP and HERA, Lund (1994);
International Workshop PHOTON-95, Sheffield, UK, 8-13 April 1995.

[5] H1 Collaboration, *Measurement of the Inclusive Di-Jet Cross-Section in Photoproduction and the Determination of an Effective Parton Distribution in the Photon*, preprint DESY-97-164, submitted to Z. Phys C.

[6] T. Uematsu and T. Walsh, Phys. Lett. **101B** (1981) 263.
T. Uematsu and T. Walsh, Nucl. Phys. **B199** (1982) 93.
G. Rossi, U. California at San Diego preprint UCSD-1-P10-227 (1983).
G. Rossi, Phys. Rev. **D29** (1984) 852.

[7] M. Glück, E. Reya and M. Stratmann, Phys. Rev. **D54** (1996) 5515.

[8] S. Frixione, M. Mangano, P. Nason and G. Ridolfi, Phys. Lett.**B319** (1993) 339.

[9] M. Klasen, G. Kramer and B. Pötter, preprint DESY 97-039, hep-ph/9703302.

[10] D. de Florian, C. Garcia Canal and R. Sassot, Z. Phys. **C75** (1997) 265.

[11] J. Chýla, J. Cvach, Proceedings of the Workshop 1995/96 on "Future Physics at HERA", eds. G. Ingelman, A. de Roeck and R. Klanner, DESY 1996, Vol. 1, p 545.

[12] M. Drees and R. Godbole, Phys. Rev. **D50** (1994) 3124.

[13] F. Borzumati and G. Schuler, Z. Phys. **C58** (1993) 139.

[14] PLUTO Collab., Ch. Berger et al., Phys. Lett. **B142** (1984) 119.

[15] H1 Collaboration, I. Abt et al., Nucl. Instr. and Meth. **A386** (1997) 310 and **A386** (1997) 348.

[16] H1 Calorimeter Group, B. Andrieu et al., Nucl. Instr. and Meth. **A336** (1993) 460.

[17] H1 Calorimeter Group, B. Andrieu et al. Nucl. Instr. and Meth. **A350** (1994) 57.
H1 Calorimeter Group, B. Andrieu et al. Nucl. Instr. and Meth. **A336** (1993) 499.

[18] H1 BEMC Group (J. Ban, et al.), Nucl. Instr. and Meth. **A372** (1996) 399.

[19] H1 SPACAL group, R. D. Appuhn et al., DESY preprint 96-171, submitted to Nucl. Instr. and Meth.

[20] H1 Collaboration, C. Adloff et al., Nucl.Phys. **B497** (1997) 3.

[21] H1 Collaboration, Technical Proposal for the Upgrade of the Backward Region of the H1 detector, DESY Internal Report, PRC-93/02.

[22] H1 Collaboration, S. Aid et al., Z. Phys. **C69** (1995) 27.

[23] H1 Collaboration, T. Ahmed et al., Nucl. Phys. **B439** (1995) 471.

[24] S. Catani, Yu.L. Dokshitzer and B.R. Webber Phys. Lett. **B285** (1992) 291.

[25] R. Engel, Z. Phys. **C66** (1995) 203;
R. Engel and J. Ranft, Phys. Rev. **D54** (1996) 4244.

[26] A. Capella et al., Phys. Rep. **236** (1994) 227.

[27] C. F. v. Weizsäcker, Z. Phys. **88** (1934) 612
E. J. Williams, Phys. Rev. **45** (1934) 729.

[28] V. M. Budnev et al., Phys. Rep. **C15** (1974) 181.

[29] T. Sjöstrand, Comp. Phys. Comm. **82** (1994) 74.
T. Sjöstrand, CERN preprint TH-7112-93 (Dec. 1993, revised Aug. 1994)

[30] G. Ingelman, Proc. of the Workshop Physics at HERA, ed W. Buchmüller and G. Ingelman, Oct. 1991, Vol. 3, 1366.

[31] L. Lönnblad, Comp. Phys. Comm. **71** (1992) 15.

[32] G. Gustafson and U. Petterson, Nucl. Phys. **B306** (1988) 746.
G. Gustafson, Phys. Lett. **B175** (1986) 453.
B. Andersson et al., Z. Phys. **C43** (1989) 625.

[33] G. Marchesini, B. Webber et al., Comp. Phys. Comm. **67** (1992) 465.

[34] G. Marchesini and B. Webber, Nucl. Phys. **B238** (1984) 1.
G. Marchesini and B. Webber, Nucl. Phys. **B310** (1988) 461.

[35] H. Jung, Comp. Phys. Comm. **86** (1995) 147.

[36] M. Glück, E. Reya and A. Vogt, Phys. Rev. **D45** (1992) 3986.

[37] T. Sjöstrand and G. A. Schuler, Phys. Lett. **B376** (1996) 193.

[38] M. Glück, E. Reya and A. Vogt, Z. Phys. **C67** (1995) 433.

[39] R. Brun et al., GEANT3 User's Guide, CERN-DD/EE 84-1, Geneva (1987).

[40] HERACLES 4.4; A. Kwiatkowski, H. Spiesberger and H.-J. Möhring, Comp. Phys. Comm. **69** (1992) 155.

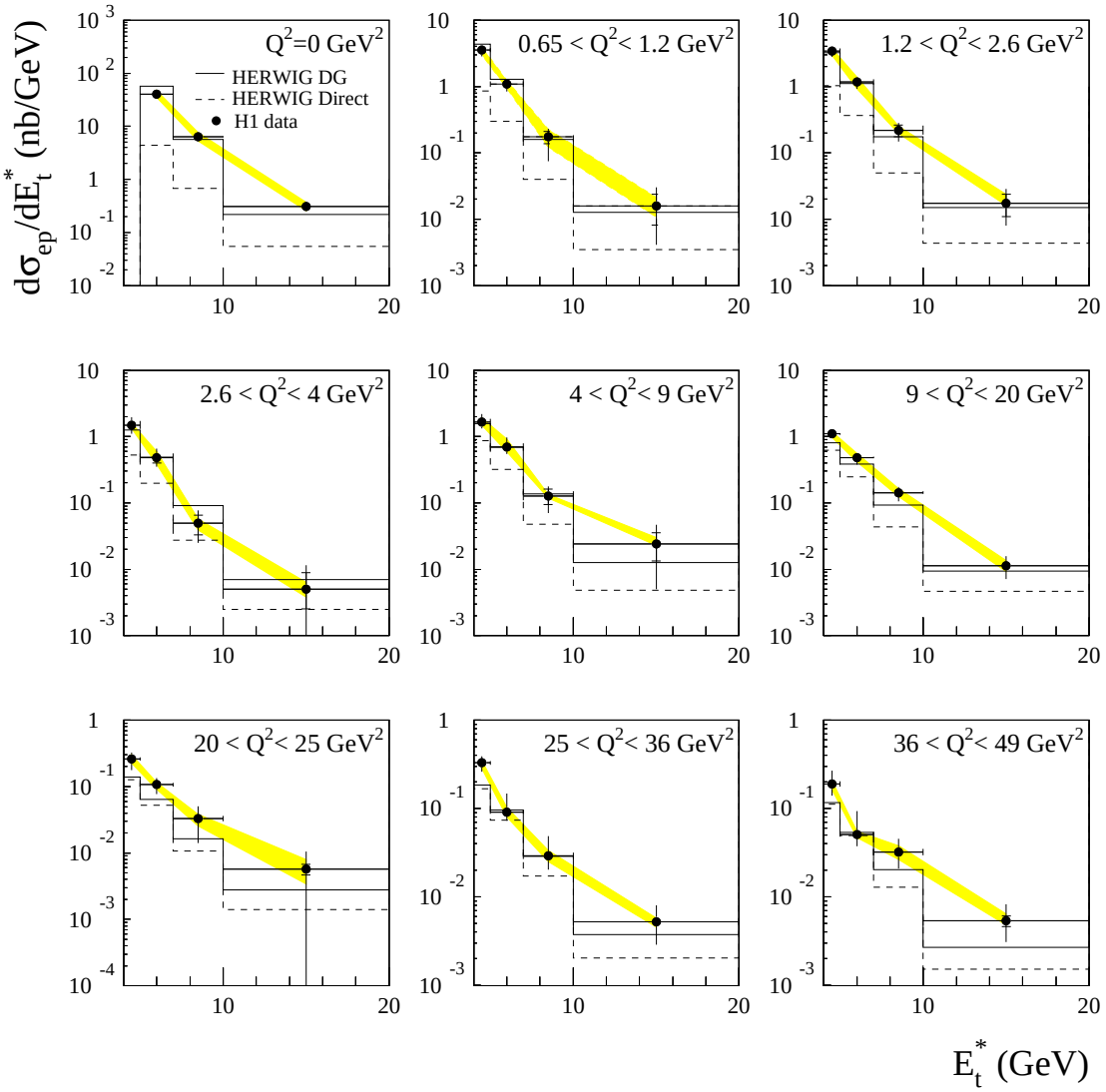

Figure 1: The differential jet cross-section $d\sigma_{ep}/dE_t^*$ for jets with $-2.5 < \eta^* < -0.5$ and $0.3 < y < 0.6$. The inner error bars indicate the statistical errors, the total error bars show the quadratic sum of the statistical and systematic errors and the shaded band represents the correlated error from the uncertainty in the Liquid Argon energy scale. Not shown is the error from the uncertainty in the luminosity determination which leads to a 3% normalisation error for the data with $0.65 < Q^2 < 9\,\mathrm{GeV}^2$ and a 1.5% normalisation error elsewhere. The data are compared to the HERWIG DG model (solid line) and to the direct contribution to this model (dashed line).

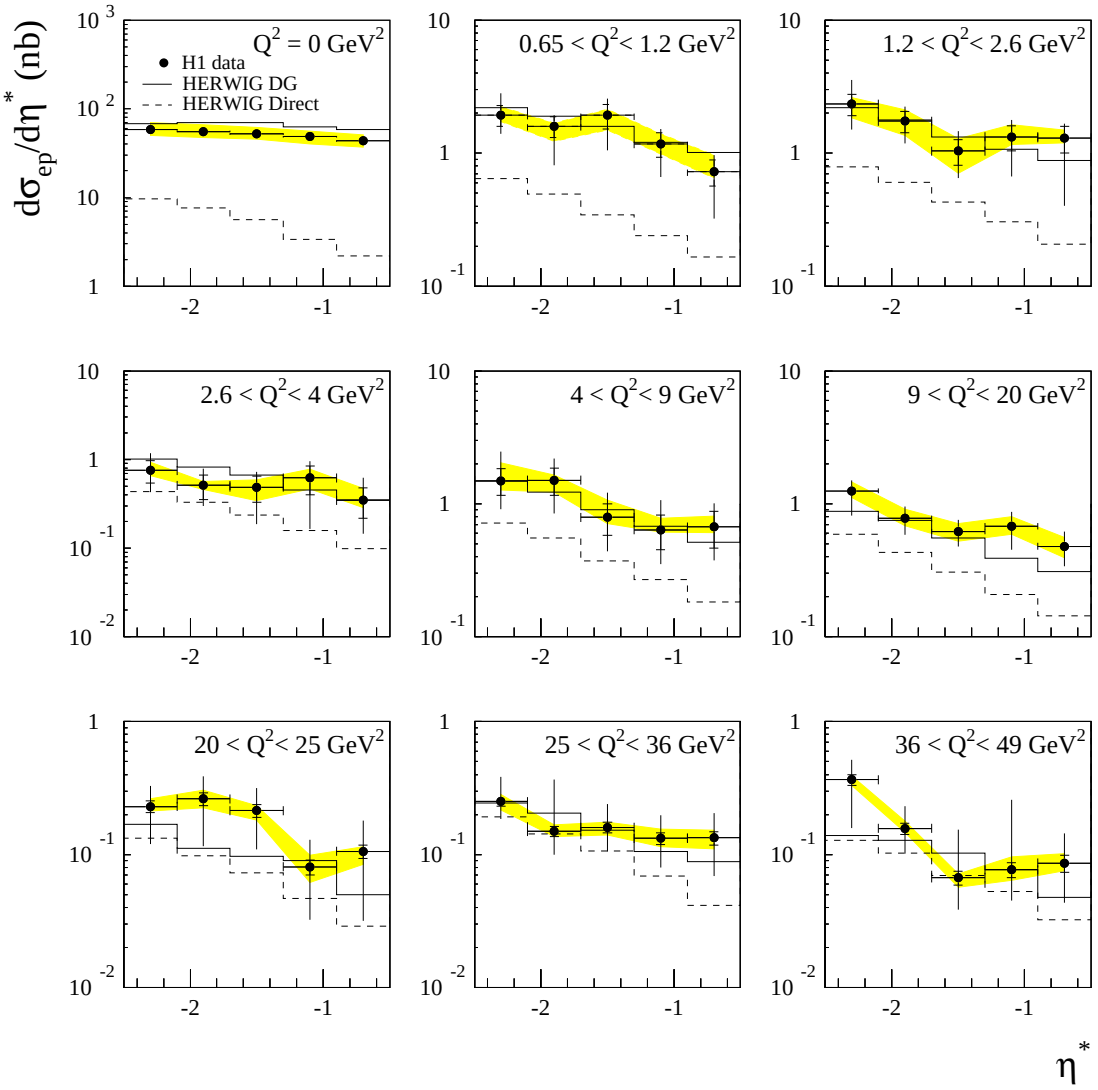

Figure 2: The differential jet cross-section $\mathrm{d}\sigma_{ep}/\mathrm{d}\eta^*$ for jets with $E_t^* > 5\,\mathrm{GeV}^2$ and $0.3 < y < 0.6$. The incident proton direction is to the right. The inner error bars indicate the statistical errors, the total error bars show the quadratic sum of the statistical and systematic errors and the shaded band represents the correlated error from the uncertainty in the Liquid Argon energy scale. Not shown is the error from the uncertainty in the luminosity determination which leads to a 3% normalisation error for the data with $0.65 < Q^2 < 9\,\mathrm{GeV}^2$ and a 1.5% normalisation error elsewhere. The data are compared to the HERWIG DG model (solid line) and to the direct contribution to this model (dashed line).

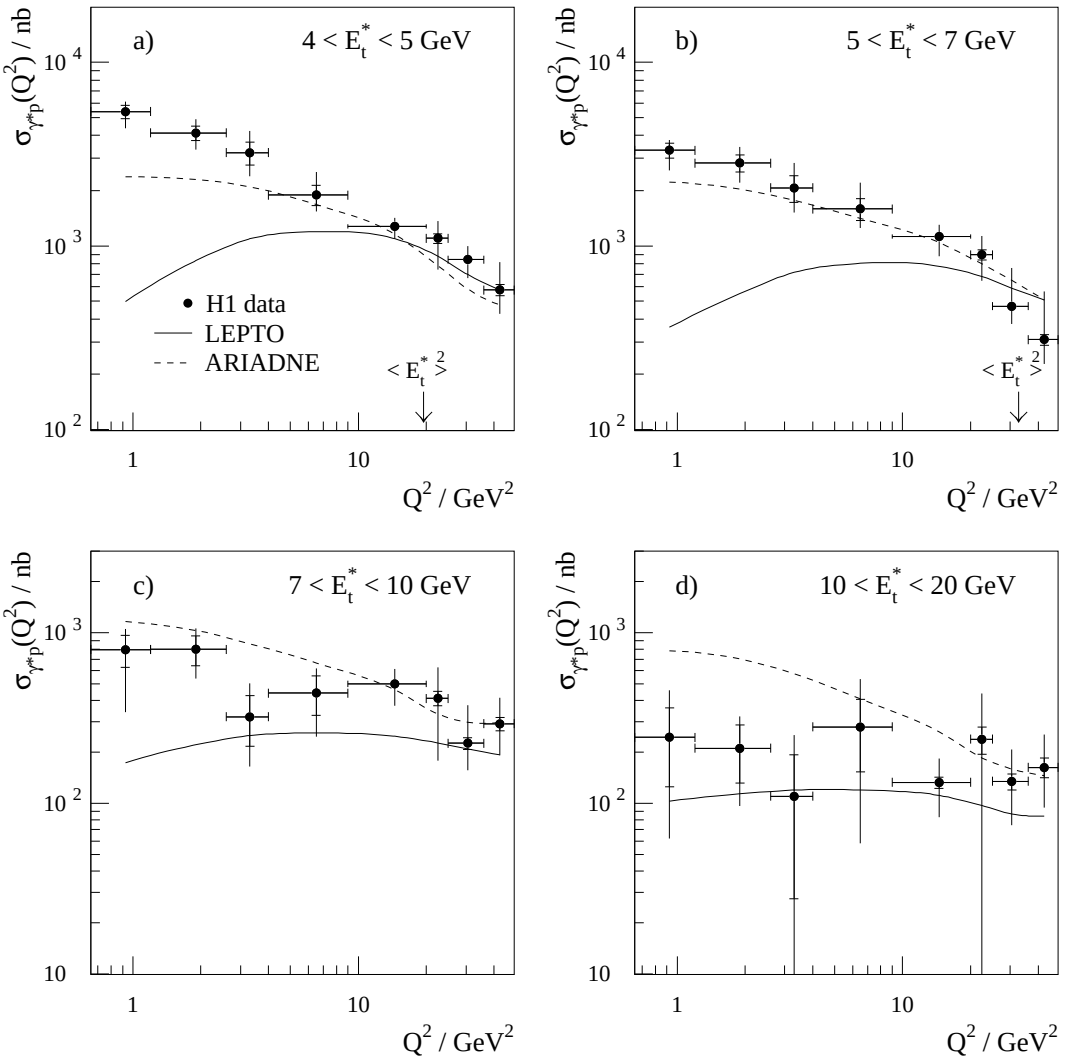

Figure 3: The inclusive $\gamma^* p$ jet cross-section $\sigma_{\gamma^* p}(Q^2)$ for jets with $-2.5 < \eta^* < -0.5$ and $0.3 < y < 0.6$. The inner error bars indicate the statistical errors and the total error bars show the quadratic sum of the statistical and systematic errors. Not shown are the normalisation error from the uncertainty in the Liquid Argon energy scale, which is 15% at low E_t^* and increases to 25% at high E_t^*, and the normalisation error from the uncertainty in the luminosity determination, which is 3% for the data with $0.65 < Q^2 < 9\,\mathrm{GeV}^2$ and 1.5% elsewhere. The data are compared to LEPTO (solid line) and ARIADNE (dashed line).

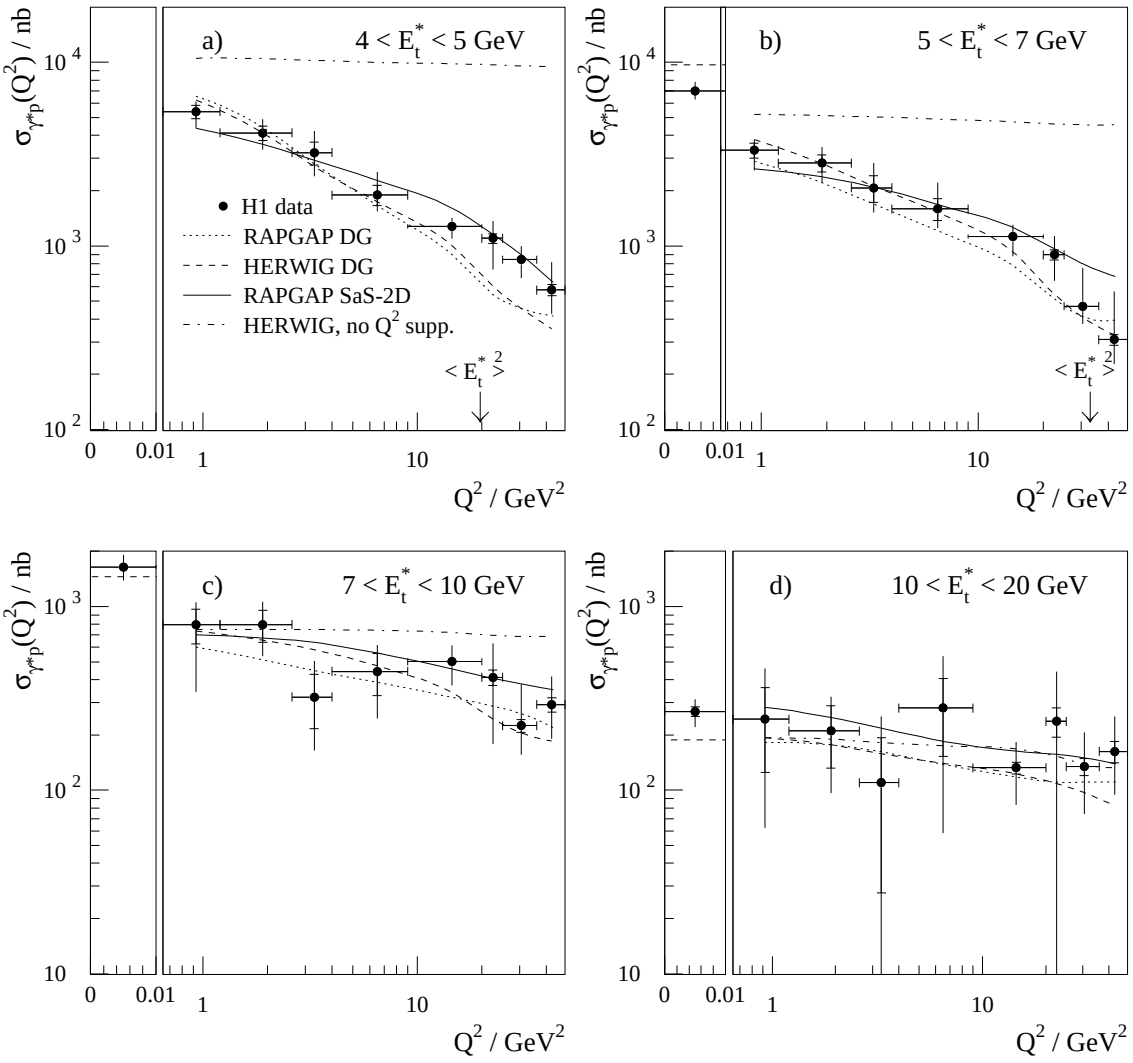

Figure 4: The inclusive $\gamma^* p$ jet cross-section $\sigma_{\gamma^* p}(Q^2)$ for jets with $-2.5 < \eta^* < -0.5$ and $0.3 < y < 0.6$. The inner error bars indicate the statistical errors and the total error bar shows the quadratic sum of the statistical and systematic errors. Not shown are the normalisation error from the uncertainty in the Liquid Argon energy scale, which is 15% at low E_t^* and increases to 25% at high E_t^*, and the normalisation error from the uncertainty in the luminosity determination, which is 3% for the data with $0.65 < Q^2 < 9\,\mathrm{GeV}^2$ and 1.5% elsewhere. The data are compared to HERWIG with no suppression of the photon structure function with Q^2 (dot–dashed line), the HERWIG DG model (dashed line), the RAPGAP DG model (dotted line) and RAPGAP with the SaS-2D photon structure function (solid line).

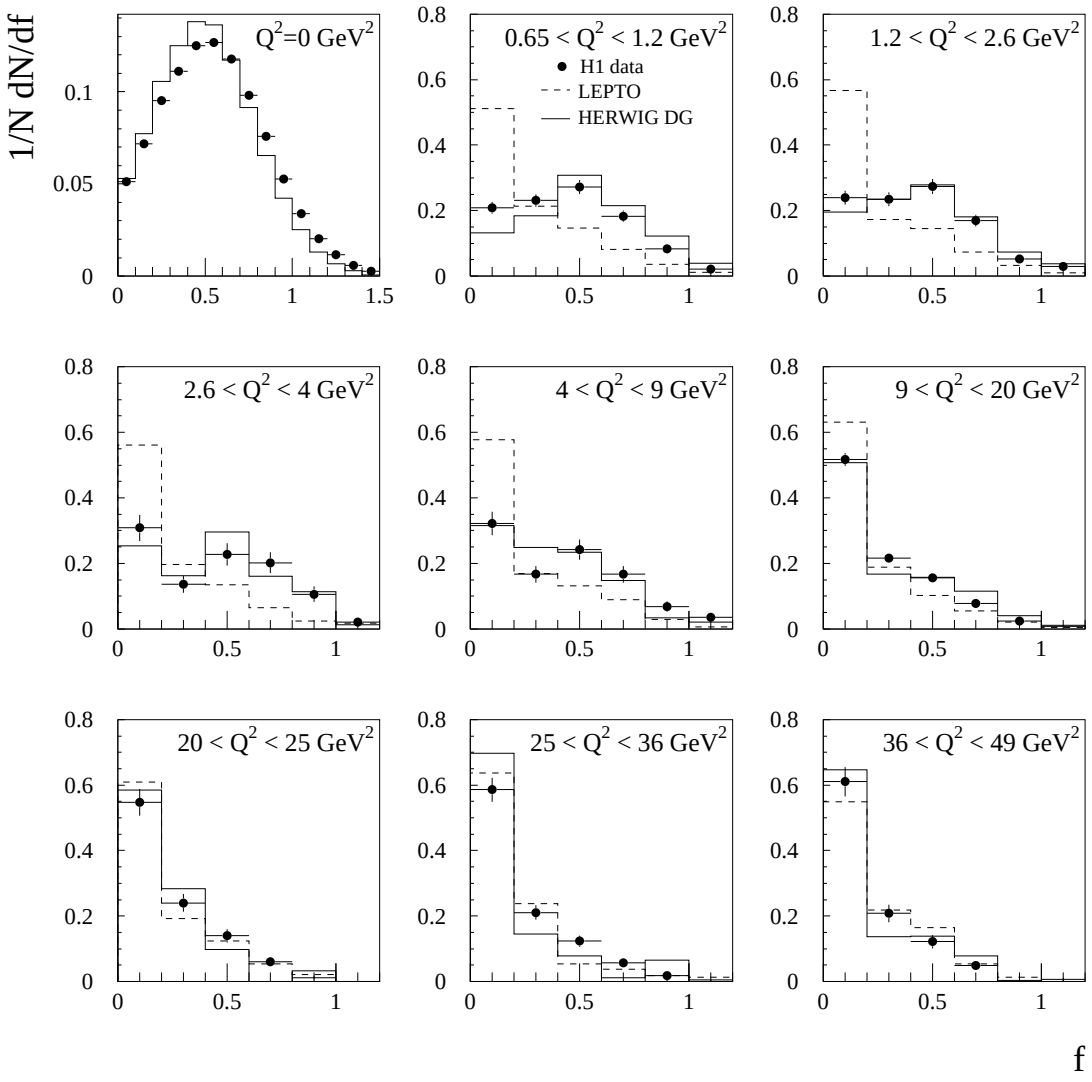

Figure 5: The uncorrected distribution of the observed fraction of the incident photon's energy which is reconstructed in the photon remnant jet (f) for events with at least one jet with E_t^* $> 5\,\mathrm{GeV}$ and $-2.5 < \eta^* < -0.5$. The data are compared to the HERWIG DG model (solid line) and to LEPTO (dashed line) after detector simulation.

Q^2 (GeV^2)	E_t^* (GeV)	$\mathrm{d}\sigma_{ep}/\mathrm{d}E_t^*$ (nb/GeV)	$\delta(stat)$	$+\delta(sys)$	$-\delta(sys)$	$\pm\delta(norm)$
$Q^2 < 10^{-2}$	$5-7$	40.7	0.5	4.8	4.0	7.1
	$7-10$	6.4	0.2	1.0	1.0	1.3
	$10-20$	0.31	0.02	0.05	0.06	0.06
$0.65 < Q^2 < 1.2$	$4-5$	3.5	0.3	0.4	0.6	0.6
	$5-7$	1.1	0.1	0.1	0.2	0.2
	$7-10$	0.17	0.04	0.04	0.09	0.05
	$10-20$	0.016	0.008	0.012	0.009	0.005
$1.2 < Q^2 < 2.6$	$4-5$	3.4	0.3	0.5	0.6	0.5
	$5-7$	1.2	0.1	0.2	0.2	0.2
	$7-10$	0.22	0.04	0.04	0.06	0.03
	$10-20$	0.017	0.007	0.009	0.007	0.007
$2.6 < Q^2 < 4$	$4-5$	1.5	0.2	0.4	0.3	0.2
	$5-7$	0.48	0.08	0.16	0.10	0.13
	$7-10$	0.049	0.016	0.023	0.018	0.008
	$10-20$	5.1×10^{-3}	3.8×10^{-3}	5.3×10^{-3}	6.9×10^{-3}	1.3×10^{-3}
$4 < Q^2 < 9$	$4-5$	1.6	0.2	0.5	0.2	0.3
	$5-7$	0.69	0.09	0.26	0.12	0.22
	$7-10$	0.13	0.03	0.04	0.05	0.01
	$10-20$	0.024	0.011	0.019	0.016	0.006
$9 < Q^2 < 20$	$4-5$	1.10	0.03	0.12	0.16	0.12
	$5-7$	0.48	0.01	0.07	0.11	0.08
	$7-10$	0.143	0.007	0.032	0.037	0.022
	$10-20$	1.13×10^{-2}	0.09×10^{-2}	0.44×10^{-2}	0.42×10^{-2}	0.23×10^{-2}
$20 < Q^2 < 25$	$4-5$	0.26	0.02	0.06	0.08	0.04
	$5-7$	0.107	0.007	0.028	0.029	0.016
	$7-10$	0.033	0.003	0.017	0.019	0.007
	$10-20$	5.7×10^{-3}	1.0×10^{-3}	4.9×10^{-3}	60.8×10^{-3}	2.3×10^{-3}
$25 < Q^2 < 36$	$4-5$	0.33	0.02	0.06	0.07	0.04
	$5-7$	0.092	0.005	0.056	0.019	0.011
	$7-10$	0.029	0.002	0.020	0.009	0.004
	$10-20$	5.2×10^{-3}	0.6×10^{-3}	2.8×10^{-3}	2.3×10^{-3}	0.7×10^{-3}
$36 < Q^2 < 49$	$4-5$	0.19	0.01	0.08	0.05	0.03
	$5-7$	0.051	0.003	0.042	0.013	0.004
	$7-10$	0.032	0.003	0.014	0.011	0.006
	$10-20$	5.4×10^{-3}	0.7×10^{-3}	3.0×10^{-3}	2.3×10^{-3}	1.1×10^{-3}

Table 2: The inclusive differential jet cross-section $\mathrm{d}\sigma_{ep}/\mathrm{d}E_t^*$ for jets with $-2.5 < \eta^* < -0.5$ in the $\gamma^* p$ centre of mass frame measured in the range $0.3 < y < 0.6$ for nine different Q^2 ranges. The statistical, positive systematic, negative systematic and normalisation errors are given. In addition, the uncertainty in the luminosity determination leads to a 3% normalisation error for the data with $0.65 < Q^2 < 9\,\mathrm{GeV}^2$ and a 1.5% normalisation error elsewhere.

Q^2 (GeV^2)	η^*	$d\sigma_{ep}/d\eta^*$ (nb)	$\delta(stat)$	$+\delta(sys)$	-$\delta(sys)$	$\pm\delta(norm)$
$Q^2 < 10^{-2}$	$-2.5 < \eta^* < -2.1$	58.6	1.4	7.9	6.8	11.6
	$-2.1 < \eta^* < -1.7$	55.8	1.3	6.8	5.8	10.3
	$-1.7 < \eta^* < -1.3$	52.4	1.2	6.3	4.6	9.7
	$-1.3 < \eta^* < -0.9$	48.9	1.1	5.4	5.5	8.3
	$-0.9 < \eta^* < -0.5$	43.6	1.0	5.5	4.4	8.5
$0.65 < Q^2 < 1.2$	$-2.5 < \eta^* < -2.1$	1.9	0.3	0.8	0.4	0.3
	$-2.1 < \eta^* < -1.7$	1.6	0.3	0.2	0.7	0.4
	$-1.7 < \eta^* < -1.3$	1.9	0.4	0.5	0.8	0.4
	$-1.3 < \eta^* < -0.9$	1.2	0.2	0.2	0.4	0.2
	$-0.9 < \eta^* < -0.5$	0.73	0.16	0.18	0.37	0.24
$1.2 < Q^2 < 2.6$	$-2.5 < \eta^* < -2.1$	2.3	0.4	1.1	0.7	0.5
	$-2.1 < \eta^* < -1.7$	1.7	0.3	0.4	0.5	0.4
	$-1.7 < \eta^* < -1.3$	1.0	0.2	0.4	0.3	0.3
	$-1.3 < \eta^* < -0.9$	1.3	0.3	0.4	0.6	0.3
	$-0.9 < \eta^* < -0.5$	1.3	0.3	0.2	0.8	0.2
$2.6 < Q^2 < 4$	$-2.5 < \eta^* < -2.1$	0.75	0.21	0.37	0.25	0.18
	$-2.1 < \eta^* < -1.7$	0.51	0.16	0.23	0.14	0.05
	$-1.7 < \eta^* < -1.3$	0.49	0.16	0.17	0.26	0.15
	$-1.3 < \eta^* < -0.9$	0.62	0.22	0.25	0.40	0.16
	$-0.9 < \eta^* < -0.5$	0.35	0.13	0.24	0.16	0.12
$4 < Q^2 < 9$	$-2.5 < \eta^* < -2.1$	1.5	0.3	0.9	0.5	0.5
	$-2.1 < \eta^* < -1.7$	1.5	0.4	0.6	0.6	0.3
	$-1.7 < \eta^* < -1.3$	0.79	0.21	0.37	0.28	0.27
	$-1.3 < \eta^* < -0.9$	0.64	0.19	0.39	0.22	0.14
	$-0.9 < \eta^* < -0.5$	0.67	0.21	0.27	0.21	0.13
$9 < Q^2 < 20$	$-2.5 < \eta^* < -2.1$	1.25	0.06	0.25	0.44	0.20
	$-2.1 < \eta^* < -1.7$	0.78	0.04	0.18	0.19	0.14
	$-1.7 < \eta^* < -1.3$	0.62	0.03	0.14	0.14	0.10
	$-1.3 < \eta^* < -0.9$	0.68	0.04	0.19	0.23	0.12
	$-0.9 < \eta^* < -0.5$	0.48	0.03	0.14	0.14	0.09
$20 < Q^2 < 25$	$-2.5 < \eta^* < -2.1$	0.23	0.02	0.10	0.11	0.03
	$-2.1 < \eta^* < -1.7$	0.26	0.03	0.13	0.15	0.04
	$-1.7 < \eta^* < -1.3$	0.21	0.02	0.10	0.11	0.03
	$-1.3 < \eta^* < -0.9$	0.08	0.01	0.05	0.05	0.02
	$-0.9 < \eta^* < -0.5$	0.11	0.01	0.07	0.07	0.02
$25 < Q^2 < 36$	$-2.5 < \eta^* < -2.1$	0.25	0.02	0.14	0.07	0.03
	$-2.1 < \eta^* < -1.7$	0.15	0.01	0.22	0.05	0.02
	$-1.7 < \eta^* < -1.3$	0.16	0.02	0.08	0.05	0.02
	$-1.3 < \eta^* < -0.9$	0.13	0.01	0.07	0.05	0.02
	$-0.9 < \eta^* < -0.5$	0.13	0.02	0.07	0.06	0.02
$36 < Q^2 < 49$	$-2.5 < \eta^* < -2.1$	0.37	0.03	0.15	0.21	0.03
	$-2.1 < \eta^* < -1.7$	0.16	0.02	0.07	0.06	0.02
	$-1.7 < \eta^* < -1.3$	0.067	0.008	0.087	0.028	0.010
	$-1.3 < \eta^* < -0.9$	0.077	0.010	0.18	0.032	0.019
	$-0.9 < \eta^* < 0.5$	0.09	0.01	0.06	0.04	0.02

Table 3: The inclusive differential jet cross-section $d\sigma_{ep}/d\eta^*$ for jets with $E_t^* > 5\,\mathrm{GeV}$ in the $\gamma^* p$ centre of mass frame measured in the range $0.3 < y < 0.6$ for nine different Q^2 ranges. The statistical, positive systematic, negative systematic and normalisation errors are given. In addition, the uncertainty in the luminosity determination leads to a 3% normalisation error for the data with $0.65 < Q^2 < 9\,\mathrm{GeV}^2$ and a 1.5% normalisation error elsewhere.